ACS MATERIALS LETTERS

www.acsmaterialsletters.org

Iron Intermediate Band Governs Relaxation Kinetics of Bornite Plasmonic Semiconductor Nanocrystals

Jason E. Kuszynski, Xingjian Zhong, Stephen A. McGill, Allison M. Dennis, and Geoffrey F. Strouse*

Cite This: *ACS Materials Lett.* 2024, 6, 3367−3375

Read Online

ACCESS | Metrics & More | Article Recommendations | Supporting Information

ABSTRACT: Intermediate band (IB) plasmonic semiconductor nanocrystals of Cu_xFeS_4 (x = 3, 5, 7) are investigated by femtosecond transient absorption (fsTA) to correlate the observed LSPR damping behavior with changes in the observed electron−phonon and phonon−phonon relaxation dynamics when excited at the localized surface plasmon resonance (LSPR) and optical band gap ($E_{g,opt}$). Changing the Cu:Fe ratio results in a shift of the Fe 3d IB consistent with an isosbestic shift seen for all fsTA data. While different relaxation pathways can be accessed, the Fe intermediate band is critical for both pump regimes, resulting in an increased hole−phonon (*ho-ph*) coupling constant as a function of increased carrier density and carrier effective mass (m^*). Additionally, evidence is provided for a correlation of LSPR m^* and damping versus *ho-ph* and *ph-ph* relaxation, respectively, by comparing fsTA data with two-temperature modeling which may be used to guide future development of high photothermal or photoacoustic conversion efficient plasmonic semiconductor nanomaterials.

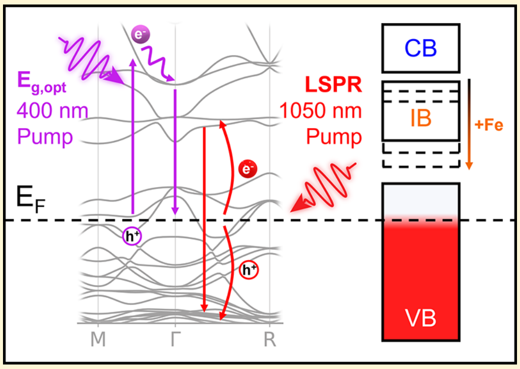

Interest in plasmonic materials is focused on the ability to enhance performance for epsilon-near-zero materials,[1−3] photothermal therapy,[4−6] electrochromic windows,[7] telecommunications,[8] infrared neural stimulation,[9−11] surface enhanced Raman scattering,[12] refractometric sensing,[13] and photocatalysis[14] by resonantly exciting the LSPR mode. The interest in plasmonic nanomaterials, whether noble metals or semiconductors, reflects the presence of a localized surface plasmon resonance (LSPR) arising from the collective oscillation of free carriers, which results in enhancement of the electric field ($\vec{E}$) in the near field.[15] Noble metals are the quintessential standard for plasmonic nanocrystal research[15−18] but are typically limited to the visible region.[19] The LSPR of plasmonic semiconductor nanocrystals (PSNCs) are widely tunable across the visible to infrared (IR) spectral region through composition, size (quantum confinement effects leading to changes in band structure),[20,21] doping,[22] and morphology.[23] The strength of the near field enhancement at the surface of a PSNC is dependent on the scattering contributions (surface, phonon, electron, and vacancy scattering). In PSNCs, nonparabolicity of the bands and aliovalent ion incorporation lead to the formation of donor−acceptor states that influence carrier density (n), effective mass (m^*), and carrier mobility (μ) by modulating electron scattering pathways. The presence of donor−acceptor states in PSNCs affects LSPR relaxation dynamics, the electronic density of states, and the applicability of PSNCs as optical materials.

While n-type, direct gap metal oxides dominate the PSNC literature, the p-type Cu_xFeS_4 (x = 3, 5, 7) bornite family, herein referred to as CFS-Cu:Fe (e.g., CFS-3:1), is an example of an intermediate band semiconductor (IBSC) that is plasmonic. IBSCs as a class of materials are increasingly being explored for their thermoelectric properties and are typically seen as indirect band gap materials, thought to make them useful toward applications in thermoelectrics and photovoltaics.[24−26] CFS PSNCs are attractive due to low elemental cost, low toxicity,[4,27] and having a biologically transmissive near-IR (NIR) plasmon frequency.[5] In CFS, the intermediate bands are composed of Fe d-orbitals that are empty due to hole doping. Manna and co-workers evaluated the relaxation processes in nanocrystal $CuFeS_2$, a related Cu−Fe−S phase having the chalcopyrite instead of the bornite

Received: February 16, 2024
Revised: June 12, 2024
Accepted: June 25, 2024
Published: July 1, 2024

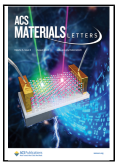

https://doi.org/10.1021/acsmaterialslett.4c00341
ACS Materials Lett. 2024, 6, 3367−3375

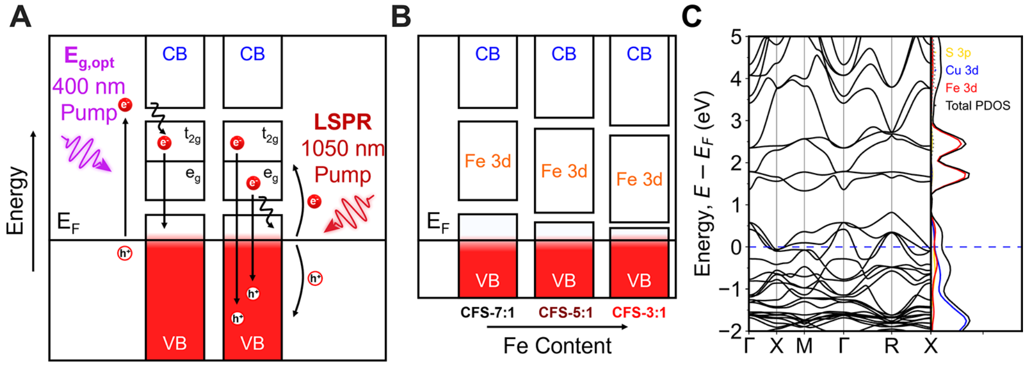

Figure 1. (A) Relaxation pathways of CFS dependent on pump energy and (B) a pictographic representation of how the Fe 3d intermediate band shifts as a function of Fe content. (C) Electronic band diagram with projected density of states of the paramagnetic CFS-5:1 unit cell for spin down electrons.

structure, and observed significant photothermal heating is caused by the Fe IB.[28] Lee et al. and Kays et al. were the first to illustrate the oxidative behavior of bornite where a high energy dielectric resonance (polaronic and chalcopyrite-like) is observed to unpin and form an LSPR at low energy.[29,30] While they performed preliminary DFT studies of the electronic band structure for bornite as a function of Fe content, there are still questions regarding how light interacts and relaxes through the density of states. While similar classes of IBSCs have been explored such as Cu_3MCH_4 and $CuFeS_2$,[28,31,32] literature of bornite, Cu_5FeS_4, is still ongoing and has been described as "puzzling".[33] To date, the band structure of bornite is still under active research, where differences in synthetic conditions can modulate the band gap from 0.5 to 1.25 eV between valence band (VB) and IB.[34,35] Overall, the results from the literature point in the direction that Fe content in the Cu−Fe−S system should directly influence the energy and population of IB states, leading to differences in relaxation dynamics.

In InN, it has been observed that simultaneous changes in m^* with n occurs, leading to the observation that LSPR frequency can remain the same even as n is reduced.[36] Furthermore, m^* is directly impacted by changes in the carrier−phonon interaction in a given material and can change with size as demonstrated in CdSe quantum dots.[37,38] Understanding how the values of n, m^*, and τ are influenced by PSNC composition is critical for tailoring the physical properties of PSNCs for future electronic and photonic applications. The LSPR frequency in CFS can be modeled using the simplified Drude model, wherein the plasma resonance frequency (ω_p) (eq 1)

$$\omega_p = \sqrt{\frac{ne^2}{m^* \varepsilon_0}} \tag{1}$$

is assumed to be primarily dependent on both n and carrier effective mass m^*, in which e is the elementary charge of an electron and ε_0 is the vacuum permittivity constant.[39] The reported p-type CFS carrier densities are on the order of 10^{21} to 10^{22} carriers based on one-electron reductant chemical titration of the LSPR extinction centered at ~9600 cm^{-1}. The change in the LSPR with Cu:Fe ratio is caused by a simultaneous modulation of n and m^* validated by chemical titration comparison to Drude model fitting of the LSPR in the 3:1, 5:1, and 7:1 compositional series.[30] The modulation of m^* is consistent with the observation of Fe vacancy population changing with Cu:Fe ratio, as evidenced by repeated observations of Fe leeching.[29,30,40] The impact of Fe vacancies is hypothesized to lead to subsequent hole pinning and polaron type carrier coupling, thus increasing the overall m^* for CFS dependent on the degree of vacancy presence and strength of carrier coupling. The effect of m^* is not only impactful on the fitting of LSPR, but it also plays a critical role in carrier mobility, μ (eq 2)

$$\mu = \frac{e\tau}{m^*} \tag{2}$$

where τ is scattering lifetime, which is impacted by carrier coupling, crystal structure defects, interstitial sites, and surface depletion effects for PSNCs.[22,41−43] While μ is difficult to measure directly in a nanocrystal, the change in LSPR relaxation dynamics provides an indirect assessment of changes in the carrier mobility with changes in Fe vacancy content. The ability to modulate the Cu:Fe ratio in CFS allows the evaluation of n, m^*, and μ in a single lattice structural type to be evaluated.

In this work, femtosecond transient absorption (fsTA) is used to explore the relationship between n, m^*, damping, and the relaxation kinetics of CFS-3:1, CFS-5:1, and CFS-7:1 in the bornite phase for the optical band gap ($E_{g,opt}$, CB to VB) versus LSPR excited pathways. Phonon−phonon (*ph-ph*) relaxation of hot holes is shown to linearly depend on LSPR damping, while hole−phonon (*ho-ph*) relaxation is observed to correlate with changes in m^* that are validated with variable field magnetic circular dichroism measurements. Additionally, the fluence-dependent measurements shed light on the interplay between carrier mobility, carrier density, and relaxation lifetimes with respect to the hole-phonon coupling constant. The Fe intermediate band is shown to play a critical role in the availability of relaxation pathways for CFS agnostic of excitation energy and can be identified by noting similarities in relaxation kinetics between LSPR and $E_{g,opt}$ pump regimes. As Fe content decreases, n and m^* simultaneously increase, resulting in improved carrier mediated thermal conductivity, which may be responsible for the enhanced performance of CFS in applications such as photoacoustic imaging and photothermal therapy.

The spherical p-type CFS samples at 3:1, 5:1, and 7:1 copper to iron were prepared as previously reported and oxidized as described in the Supporting Information.[30] The CFS nanocrystals are isolated as nanocrystals passivated by oleic acid and are of cubic bornite crystal type. The LSPR

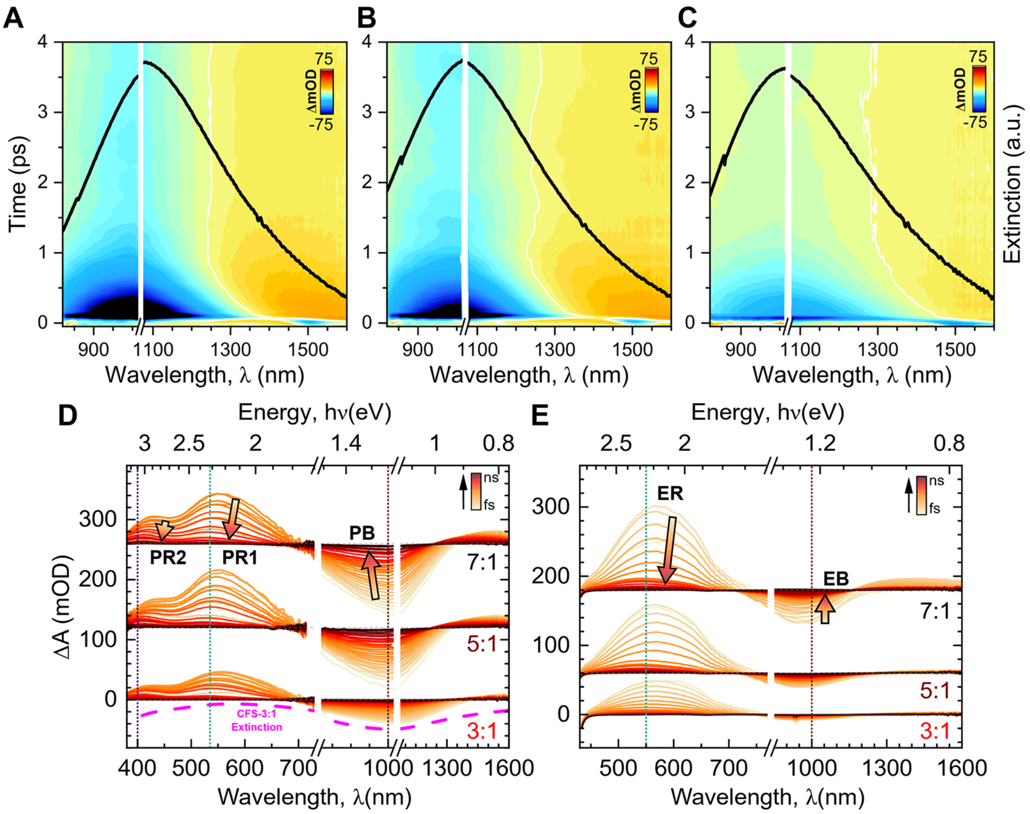

Figure 2. Characteristic two-dimensional transient absorption maps of (A) CFS-7:1, (B) CFS-5:1, and (C) CFS-3:1 with the steady-state extinction spectrum overlaid on top in black and $\Delta m_{OD} = 0$ indicated by a white line. (D) LSPR pumped (1.18 eV, 1050 nm) fsTA spectra for Cu$_x$FeS$_4$ (x = 3,5,7) are compared, all displaying two characteristic PIA features assigned to IB-II (PR2) and IB-I (PR1) relaxation transitions, where the first is observed near 2.9 eV and the second near 2.2 eV. When a near-infrared (NIR) probe pulse is used, the LSPR bleach is observed (PB) centered near 1.1 eV, qualitatively matching the LSPR extinction spectrum (pink dotted line). Additionally, intraband PIA transitions are observed for all samples below 1.0 eV. (E) $E_{g,opt}$ pumped (3.1 eV, 400 nm) fsTA spectra for all CFS are also compared, all displaying one characteristic PIA feature assigned to a IB-II → VB relaxation transition (ER) centered near 2.2 eV. The NIR probe of $E_{g,opt}$ pumped fsTA showcases one GSB assigned to IB-I depopulation (EB) while the low energy PIA is attributed to intraband relaxation.

frequency for all three samples is located between 1000 to 1100 nm, shifting to lower energy with increasing Cu:Fe ratio, shown in Figure S1. The observed composition-dependent LSPR shift was previously attributed to a combined change of carrier density and carrier effective mass with CFS-7:1 having both the highest *n* and *m**, while CFS-3:1 has the lowest *n* and *m** based on simple Drude approximation (SDA) fitting.[30] The Fermi level (E_F) is observed to be within the valence band, in agreement with the p-type, hole-based LSPR assignment. Additionally, the Fe intermediate bands are adjacent and slightly overlapping with the conduction band. The IB can be broken down into two regimes, IB-II and IB-I with higher and lower energies, respectively. Due to the tetrahedrally coordinating Fe site in bornite, IB-II and IB-I are also assigned as the Fe t_{2g} and e_g levels, respectively, as previously reported.[44] While the crystallographic structure of the CFS family is identical (Figure S1) and each possess an identifiable LSPR, the relaxation dynamics from LSPR excitation are anticipated to differ due to changes in scattering contributions from hole-phonon (*ho-ph*) and phonon−phonon (*ph-ph*) processes as well as compositionally induced changes to the density of states leading to modification of hot carrier relaxation pathways into the electronic manifold and lattice phonon bath.

The relaxation pathways for LSPR and optical band gap ($E_{g,opt}$) pumped CFS samples are schematically illustrated in Figure 1A. As the Fe content in CFS changes, it is expected that intermediate band Fe levels will decrease in energy with respect to E_F, as represented in Figure 1B. This also causes the VB to shift lower in energy, resulting in a decrease in hole carriers. The electronic band diagram with projected density of states for paramagnetic, spin-down CFS-5:1 is shown for reference in Figure 1C with k-space dependence of the bornite IBSC arising from empty tetrahedrally coordinating Fe sites in bornite. The Fe t_{2g} and e_g levels that comprise the intermediate band are herein referred to as IB-II and IB-I, respectively, identified and assigned as previously reported.[29,44] As observed in the computational band diagram, the Fe intermediate bands are predicted to be adjacent and slightly overlap with the conduction band.

In Figure 2A−C, a color contour plot overlapped with the LSPR extinction spectra for each CFS ratio is shown along with the femtosecond transient absorption spectral map for LSPR (1.18 eV, 1050 nm) and $E_{g,opt}$ (3.1 eV, 400 nm) pump regimes in Figure 2D, E. The ground state spectrum can be described by a NIR LSPR mode at ∼1100 nm and UV−vis features attributed to optical band gap ($E_{g,opt}$), intermediate band, and ligand passivation layer absorption. Figure 2A−C qualitatively highlights the increased O.D. response with

Table 1. Bi-exponential Lifetimes and Populations for All Identified LSPR Pumped fsTA Features

1050 nm pump		material		
probe feature (nm)	lifetime	CFS-7:1	CFS-5:1	CFS-3:1
(PR2) 400	τ_1 (fs)	568 ± 23 (84.2%)	573 ± 76 (79.9%)	641 ± 21 (89.9%)
	τ_2 (ps)	20.2 ± 0.5 (15.8%)	17.4 ± 1.1 (20.7%)	14.3 ± 0.4 (10.1%)
(PR1) 535	τ_1 (fs)	371 ± 6 (98.8%)	387 ± 5 (98.0%)	376 ± 7 (99.5%)
	τ_2 (ps)	20.9 ± 0.6 (1.2%)	19.6 ± 0.5 (2.0%)	13.8 ± 0.3 (0.5%)
(PB) 1000	τ_1 (fs)	434 ± 5.1 (91.7%)	472 ± 8.9 (90.8%)	499 ± 9.1 (93.7%)
	τ_2 (ps)	25.1 ± 1.9 (8.3%)	27.0 ± 3.3 (9.2%)	20.5 ± 3.3 (6.3%)

Table 2. Bi-exponential Lifetimes and Populations for All Identified $E_{g,opt}$ Pumped fsTA Features

400 nm pump		material		
probe feature (nm)	lifetime	CFS-7:1	CFS-5:1	CFS-3:1
(ER) 550	τ_1 (fs)	656 ± 18 (93.0%)	690 ± 20 (92.0%)	747 ± 20 (88.5%)
	τ_2 (ps)	28.1 ± 6.4 (7.0%)	29.3 ± 6.5 (8.0%)	18.5 ± 2.3 (11.5%)
(EB) 1000	τ_1 (fs)	523 ± 20 (90.3%)	594 ± 24 (87.6%)	620 ± 30 (92.8%)
	τ_2 (ps)	24.8 ± 2.8 (9.7%)	36.9 ± 4.9 (12.4%)	15.1 ± 3.1 (7.2%)

decreased Fe content in fsTA measurements, which corresponds with a decrease in LSPR damping and subsequent increased electric field enhancement with LSPR pumping.

The LSPR pumped fsTA spectra (Figure 2D) for the three CFS samples can be deconvolved into three photoinduced absorptions (PIA) and one ground state bleach (GSB). The fsTA spectra are spectrally similar regardless of changing Cu:Fe ratio, but energy shifts observed for all features are consistent with the different shifts in the linear absorption spectra reflecting the shifting Fe IB and LSPR frequency. For all spectra, there is also a small hypsochromic shift occurring over long time, as observed in the TA data for WO_{3-x} PSNCs.[45] The LSPR pumped PIA transitions are assigned to intermediate band relaxation of LSPR generated hot holes from IB-II and IB-I to the ground state, labeled PR2 and PR1, respectively. The GSB is identified as the LSPR bleach due to its matching profile with steady-state extinction spectra and labeled PB. Inspection of the 2D plots show the expected shift in the energy for PR2 and PR1 based on the energy shift of Fe IBs as a function of Fe content, recalling Figure 1B. Likewise, PB and the low energy intraband PIA shift proportionally reflecting differences in n and m^*. To verify the assignment of hot hole relaxation for PR2 and PR1, the change in spectral and temporal relaxation dynamics for the PIAs was measured following the addition of a sacrificial reductant, EtOH. The EtOH decay dynamics and kinetics of CFS-3:1 are shown in Figure S2. Upon addition of EtOH, a new, broad GSB growing at long times is assignable to the trapping of hot hole species by EtOH. Trapping of the hot hole prevents the ground state of CFS from fully recovering within 1 ns. The observed response to EtOH is consistent with behavior reported for CuS with the addition of alkanethiol as a hole acceptor, where a long time GSB was also observed at times longer than 20 ps.[46] The kinetics of all other identified features are invariant with the addition of EtOH, meaning that only PR2 and PR1 transitions possess hot enough holes to be captured by EtOH.

Biexponential kinetics for the LSPR pumped regime are tabulated in Table 1 while kinetic fits are shown in Figure S3A,B. Steady-state LSPR spectral features (plasmon damping (Γ), plasmon frequency (ω_{LSPR}), n, and m^*) are compiled in Table S1 based on the CFS PSNCs measured in this study and in a previous publication.[30] Observation of biexponential decays for LSPR pumped CFS is consistent with earlier fsTA data obtained for ICO, $Cu_{2-x}S$, and WO_{3-x}, where fsTA dynamics are typically identified by a three-step process which includes $a < 100$ fs carrier−carrier formation called Landau damping, followed by LSPR electronic relaxation via carrier−phonon scattering, followed by phonon−phonon thermalization undergone within the nanocrystal lattice.[45−49] As CFS features a hole (*ho*) majority LSPR, the decay dynamics are described as hole−phonon (*ho-ph*, τ_1) and phonon−phonon (*ph-ph*, τ_2) relaxation. Inspection of the lifetime data for the CFS samples in Table 1 reveals that overall, as the Fe content increases, τ_1 is observed to increase in lifetime, while τ_2 tends to decrease. The increase in τ_1 is consistent with an overall decrease in both n and m^*, where less scattering centers leads to an increase in mean free path and carrier lifetime and a lower m^* represents less coupling of the carrier to external forces which could cause it to relax faster. PR2 and PR1 have τ_2 lifetimes that are comparable across the CFS series, while PR2 has nearly double the τ_1 lifetime compared to PR1. As IB-I is on resonance with the LSPR, it is expected that free holes localized in IB-I experience an overall greater density of hole scatterers with the concomitant restoration of hole population for the LSPR immediately after excitation, resulting in a faster τ_1 for PR1 compared with PR2. The observed decay dynamics for PR1 τ_2 are strongly correlative with the steady-state LSPR damping (Γ) observed in extinction spectroscopy (Figure S4, $R^2 = 1.0000$). The observation of a strong correlation is reasonable, as higher Γ equates to higher carrier scattering in the PSNC dictated by a combination of bulk, surface, and chemical interface terms.[50] Therefore, the observation of faster *ph-ph* relaxation serves as a proxy for Γ. This association can also be attributed to the LSPR energy being on resonance with the IB-I intermediate band, and therefore, it is likely the most sensitive to the lattice scattering that originates from Fe t_{2g}. While the PR2 transition τ_2 is also correlative ($R^2 = 0.9588$), it does not have a linear relationship as strong as that observed for the PR1 transition.

In Figure 2E, the $E_{g,opt}$ fsTA spectra exhibit a similar spectral pattern, however with only 2 PIAs and one GSB. Most notably, there is no evidence of a higher energy PIA in the $E_{g,opt}$ spectra, and the GSB is blue-shifted, centered near 900 nm. The high energy PIA does undergo a long-time hypsochromic shift; however, the GSB does not shift in energy, indicating that the transition is fundamentally different from the previously LSPR pumped GSB. The $E_{g,opt}$ pumped regime PIA and GSB are assigned to intermediate band relaxation of IB-II to VB and IB-I bleaching, labeled ER and EB respectively. Although the energy of ER is lower than that of PB2 by ∼0.7 eV, it is important to remember that fsTA monitors the energy differences that arise from transitions and not an energy with respect to E_F or the ground state. Because the LSPR generates hot holes and electrons deep within the VB and in the IB, respectively, the energy difference that can be achieved between hot hole and electron recombination is much greater than the pump energy limited $E_{g,opt}$ excitation, as illustrated in Figure 1A. The 2.2 eV ER transition is the expected energy from E_F to IB-II in Figure 1C and is, therefore, assigned as the IB-II to VB transition.

The $E_{g,opt}$ pumped regime also exhibits biexponential decay kinetics, shown in Table 2 and plotted in Figure S3C,D. For the $E_{g,opt}$ pumped regime, the PIA at an energy near the IB-I to VB transition has distinctly different relaxation kinetics than observed in LSPR pumped. τ_1 is comparable to the PR2 transition, as carriers for both processes encounter the same Fe 3d t_{2g} orbital environment while encountering similar kinetic changes with changing Cu:Fe ratio. The IB-II to VB assignment of ER is supported by noting the increasing isosbestic point as a function of increasing Cu:Fe ratio, where it is expected that the isosbestic energy of ER shifts to higher energy as Fe content decreases, as shown in Figure 1B. The identity of EB is less straightforward. The observed offset of EB relative to PB in the fsTA data is suggestive of either a photodoping phenomenon previously observed for n-type plasmonic systems due to interband excitation[1,47,51,52] or could be depopulation of the underlying IB-I transitions that is otherwise dominated by the LSPR extinction feature. Considering that at long times the LSPR does not relax to the energy of the LSPR, photodoping seems unlikely in this case, and therefore, the assignment of an IB-I bleach transition is made for EB. ER and EB τ_1s show the same Fe content dependence as the LSPR pumped regime, where lifetime increases with greater Fe content, likely also due to n and m^* changes as discussed previously, as the presence of hole free carriers should still impact exciton recombination.

It is not surprising that a strong correlation between the relaxation dynamics and CFS composition is observed. The correlation is anticipated to extend to the m^* values and *vide infra* to the observed LSPR damping constant (Γ). Variable field magnetic circular dichroism (VH-MCD) was performed on all CFS to optically probe m^* as a function of the applied magnetic field. Details of the fitting procedure are discussed in other works and in the Supporting Information.[44] Figures 3 and S5 showcase the composition dependent m^* results and raw VH-MCD spectra respectively, where m^* for CFS-5:1 is reproduced from literature.[44] CFS-3:1 and CFS-7:1 display no magnetic field dependent m^* but can be averaged over magnetic field strengths to obtain m^*/m_e values of 1.56 ± 0.10 and 2.00 ± 0.16, respectively, shown in Figure 3. The VH-MCD m^* values track reasonably well with the SDA extracted values, with a small scalar difference of ∼0.5. Table S1 compares the simple Drude approximation extracted m^* with MCD obtained m^*. Assuming the linear relationship between CFS samples from the Drude results is consistent with the MCD results, an interpolated m^* of 1.74 is extracted for CFS-5:1, as the magnetic field-dependence of CFS-5:1 prevents a reliable extraction of a zero-field m^* for comparison, but the deviation from the experiment may explain why CFS-5:1 deviates the most from the PB linear correlation in Figure S4 (R^2 = 0.6918). Interestingly, the deviation in m^* is reminiscent of a previous report where p-type $Cu_{2-x}Se$ m^* from MCD versus bulk was measured to have a similar 0.5 m^*/m_e difference.[53] From these results, it would be worthwhile to carefully examine why these copper based PSNCs are repeatedly observed to have some offset from bulk or Drude analyzed results.

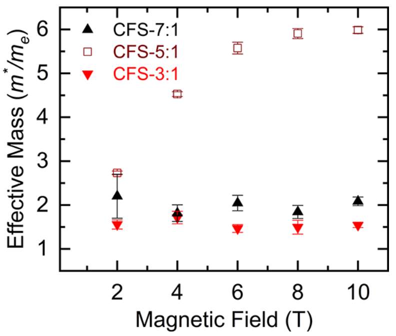

Figure 3. VH-MCD for all three bornite ratios (CFS-7:1, 5:1, 3:1 from top to bottom respectively) were fit with simulated MCD spectra to obtain a Zeeman splitting energy for all collected fields. CFS-3:1 and CFS-7:1 show no field-dependent m^* behavior and are thus averaged to obtain m^*/m_e values of 1.56 and 2.00, respectively. (CFS-5:1 data is reproduced with permission from ref 44. Copyright 2022 American Chemical Society.)

The free carriers that constitute the LSPR are also descriptive of the electronic properties of the host nanocrystal as well. To this end, a comparison of LSPR m^* and Γ can be analyzed relevant to the *ho-ph* and *ph-ph* relaxation lifetimes (Figure S4). Remarkably, there is a linear correlation observed for a majority of the relaxation pathways observed for both the LSPR and $E_{g,opt}$ pumped regimes. *Ho-ph* relaxation tracks with m^* as the mobility of free carriers are directly correlated with their lifetime, as shown previously in eq 2. Considering that carrier scattering in this size regime has an up to 49% chemical interfacing damping component,[50] it is unsurprising that *ph-ph* relaxation tracks well with overall LSPR damping due to the coupling of host nanocrystal with surrounding passivating ligands and solvent medium thermalization.

The degree of hot carrier relaxation as a function of CFS composition can be evaluated by using the PB fluence dependence. The biexponential fits are shown in Figure S6 for the power dependent response and lifetimes are plotted in Figure 4A. From the fluence dependence, a *ho-ph* relaxation rate at zero fluence (τ_0) can be extracted for all CFS which allows for the calculation of a hole-phonon coupling constant, G, analogous to the electron-coupling constant previously obtained by Milliron and co-workers for plasmonic systems.[54] Using eqs 3 and 4

$$\frac{\gamma_1}{\gamma_2} = \frac{m_1\sqrt{n_1}}{m_2\sqrt{n_2}} \tag{3}$$

$$\tau_0 = \frac{\gamma T_0}{G} \tag{4}$$

G and γ, hole heat capacity, can be calculated by using the known n, m^*, and γ from other plasmonic systems, such as Au or Ag, and are used to calculate γ for CFS in comparison to gold nanoparticles (AuNPs) where subscript 1 represents a

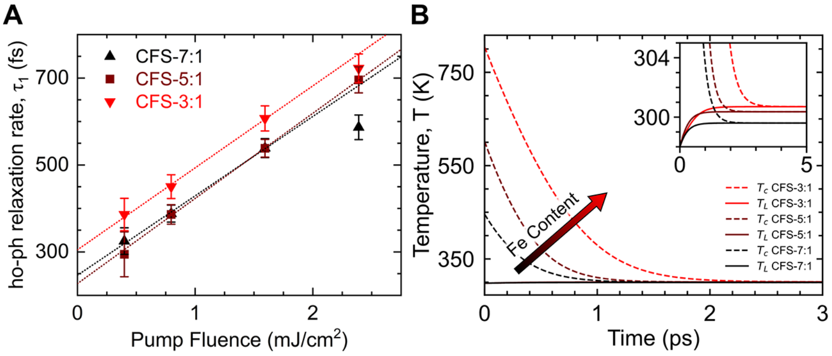

Figure 4. (A) Fluence dependent measurements are performed for all CFS samples, where τ_0s are obtained from linear fits of the three lowest fluences. The τ_0s obtained are 304, 227, and 246 fs for CFS-3:1, CFS-5:1, and CFS-7:1, respectively. Once the *ho-ph* coupling constant is calculated using τ_0, (B) the TTM is used to compare carrier and lattice temperature as a function of time using 100 μJ/cm^2 photon incidence for all CFS samples. From the model, a clear trend between Fe content and *ho-ph* relaxation is observed where CFS-3:1 is predicted to have the longest *ho-ph* relaxation and greatest lattice temperature increase of all samples.

known material and subscript 2 an unknown material. T_0 is the temperature of the PSNC environment (T_0 = 298 K)

For all CFS samples, G is observed to be higher than previously measured AuNPs,[55] which may partially contribute to the 5-fold signal increase in photoacoustic imaging signal observed by CFS-5:1 compared to AuNPs.[56] Interestingly, as the Fe content decreases, notable increases in G and γ are observed for the CFS system. This trend reflects the increase in n and m^* as the Fe content decreases from CFS-3:1 to CFS-7:1. With greater n, a greater number of hot holes can be produced with LSPR excitation, and thus, a greater amount of heat can be dissipated and relaxed through the lattice of CFS nanocrystals. Additionally, with greater m^*, the greater holes couple with the nanocrystal lattice; therefore, they can more efficiently conduct heat. Applying the two-temperature model (TTM) to the experimental data provides further insight into the interaction of the CFS hot carriers and the lattice relaxation pathways as reported by carrier and lattice temperature (T_c, T_L). TTM is a popular approach to model plasmonic systems and is performed by solving for a pair of differential equations (eqs 5 and 6)[1,54,57]

$$\gamma T_c \frac{\mathrm{d}T_c}{\mathrm{d}t} = -G(T_c - T_L) \tag{5}$$

$$C_p \frac{\mathrm{d}T_L}{\mathrm{d}t} = G(T_c - T_L) \tag{6}$$

where C_p is the material bulk heat capacity. For CFS, C_p is calculated by using the room temperature result of heat capacity from Robie et al.[58] and converting to units of J K^{-1} cm^{-3} using the density of bornite and the stoichiometric molar mass dependent on Fe content. The G and γ parameters are listed in Table 3. As Fe content increases for equal photon absorption and volume fraction, Figure 4B shows an increase in the lifetime of *ho-ph* relaxation, analogous to the trends observed in fsTA for τ_1 for all regimes. The long time T_L is shown to have a greater baseline as Fe increases as well, indicative of greater lattice heating, supporting claims by this work and others[28,29] indicating that the Fe IB indeed plays a critical role in the photothermal effects of CFS.

Table 3. Hole−Phonon Coupling Parameters for CFS Samples Compared with AuNPs from Literature

parameter	CFS-3:1	CFS-5:1	CFS-7:1	AuNPs[55]
τ_0 (fs)	304	227	246	650
γ (J K^{-2} cm^{-3}) (×10^{-5})	3.21	4.29	5.79	5.88
G (J K^{-1} s^{-1} cm^{-3}) (×10^{10})	3.14	5.63	7.01	2.70

Excitation of the LSPR and $E_{g,opt}$ leads to discrete relaxation pathways as shown in Figure 1A. A study on p-type CuS observed a similar bimodal fsTA spectrum with opposite relative intensities.[46] In CuS, an isosbestic points at the edges of their fsTA spectra, and the formation of new excited state species after 2 ps was observed. For the CFS materials, we observe no later speciation occurring; rather, all excited states appear to decay concomitantly. Additionally, the isosbestic points in this work shift as a function of time from low to high energy, also indicative of hot carrier relaxation as observed previously in WO_{3-x}, shifting within several ps and stabilizing at long time.[45] These observations in CFS points to a different relaxation pathway rather than the S- or ligand-based hole trapping in a defect state lying between CB and VB, as suggested in CuS.[46] Rather, the concomitant decay across the entire spectrum implies that there are no new species formed (i.e., no trap sites), and instead the intermediate band serves as a carrier sink for electronic and thermal relaxation. Consistent with this, the experimental data supports a shift in the intermediate bands as a function of the Cu:Fe ratio, with the Fe 3d IB shifting to higher energy with respect to the CB and E_g.

For the first time, a plasmonic p-type IBSC system has been investigated for its ultrafast relaxation pathways in the LSPR versus $E_{g,opt}$ pumping regimes. From this work, it is confirmed that the Fe IB plays a critical role in allowing both hot holes and excitonic carriers to relax back to the ground state. The hole−phonon coupling constants for CFS as a function of Fe content were calculated from fluence dependent measurements, where CFS-7:1 had the highest G due to having the greatest carrier density and carrier effective mass. The TTM was performed from the calculated G and γ parameters, providing additional explanation as to why an increase in the lifetime is concomitantly observed with increasing Fe content. Additionally for the first time, a correlation was made between LSPR m^* and damping with *ho-ph* and *ph-ph* relaxation respectively. This work paves the way for further investigation of p-type IBSC materials, where applications that require high m^* values, such as photoacoustic imaging and photothermal therapy, may be further improved.

■ ASSOCIATED CONTENT

Supporting Information

The Supporting Information is available free of charge at https://pubs.acs.org/doi/10.1021/acsmaterialslett.4c00341.

> Steady-state optical and structural characterization of CFS; LSPR Pump, UV−vis probe for CFS-3:1 with EtOH added; excited state kinetics of LSPR and $E_{g,opt}$ Pumped CFS; steady-state LSPR parameters compared to MCD derived m^*; tracking Drude properties with relaxation lifetimes; magnetic circular dichroism measurements of all CFS; and fluence dependent kinetics of LSPR bleach for all CFS samples (PDF)

■ AUTHOR INFORMATION

Corresponding Author

Geoffrey F. Strouse − *Department of Chemistry and Biochemistry, Florida State University, Tallahassee, Florida 32306, United States;* orcid.org/0000-0003-0841-282X; Email: gstrouse@fsu.edu

Authors

Jason E. Kuszynski − *Department of Chemistry and Biochemistry, Florida State University, Tallahassee, Florida 32306, United States;* orcid.org/0000-0002-9458-6940

Xingjian Zhong − *Department of Biomedical Engineering, Boston University, Boston, Massachusetts 02215, United States; Department of Chemical Engineering, Northeastern University, Boston, Massachusetts 02215, United States*

Stephen A. McGill − *National High Magnetic Field Laboratory, Tallahassee, Florida 32310, United States*

Allison M. Dennis − *Department of Chemical Engineering, Northeastern University, Boston, Massachusetts 02215, United States;* orcid.org/0000-0001-5759-9905

Complete contact information is available at: https://pubs.acs.org/10.1021/acsmaterialslett.4c00341

Author Contributions

CRediT: **Jason E. Kuszynski** conceptualization, data curation, formal analysis, investigation, methodology, project administration, software, validation, visualization, writing-original draft, writing-review & editing; **Xingjian Zhong** resources, validation, writing-review & editing; **Stephen A. McGill** methodology, resources, supervision, writing-review & editing; **Allison M. Dennis** funding acquisition, resources, supervision, writing-review & editing; **Geoffrey F. Strouse** conceptualization, funding acquisition, project administration, supervision, writing-original draft, writing-review & editing.

Notes

The authors declare no competing financial interest.

■ ACKNOWLEDGMENTS

G.F.S. and J.E.K. are grateful for the financial support provided by the National Science Foundation under grant number DMR-1905757, “Tuning Plasmonic and Magneto-Plasmonic Behavior in 4-d Transition Metal Doped Indium Oxide”. The X-ray Crystallography Center (FSU075000XRAY) and the Materials Characterization Laboratory (FSU075000MAC) at the FSU Department of Chemistry and Biochemistry are acknowledged for providing valuable resources for this research. J.E.K. thanks the Department of Defense for funding through the SMART Scholarship under OUSD/R&E, NDEP/BA-1. A.M.D. and X.Z. thank the National Institute of General Medical Sciences of the National Institutes of Health under Award Number R21GM135849 for funding. A portion of this work was performed at the National High Magnetic Field Laboratory, which is supported by the National Science Foundation Cooperative Agreement (DMR-1644779) and the state of Florida. Gratitude is expressed to Dr. Carl Conti III for the collection of initial UV−vis probe fsTA data.

■ REFERENCES

(1) Diroll, B. T.; Guo, P.; Chang, R. P. H.; Schaller, R. D. Large Transient Optical Modulation of Epsilon-Near-Zero Colloidal Nanocrystals. *ACS Nano* **2016**, *10*, 10099−10105.

(2) Reshef, O.; De Leon, I.; Alam, M. Z.; Boyd, R. W. Nonlinear optical effects in epsilon-near-zero media. *Nat. Rev. Mater.* **2019**, *4*, 535−551.

(3) Li, C.; Tian, X.; Yang, G.; Dev, S. U.; Allen, M. S.; Allen, J. W.; Harutyunyan, H. Invertible optical nonlinearity in epsilon-near-zero materials. *Phys. Rev. Research* **2023**, *5*, 013198.

(4) Wang, D.; Zhang, Y.; Guo, Q. Sub-10 nm Cu5FeS4 cube for magnetic resonance imaging-guided photothermal therapy of cancer. *Int. J. Nanomedicine* **2018**, *13*, 7987−7996.

(5) Yuan, L.; Hu, W.; Zhang, H.; Chen, L.; Wang, J.; Wang, Q. Cu5FeS4 Nanoparticles With Tunable Plasmon Resonances for Efficient Photothermal Therapy of Cancers. *Front Bioeng Biotechnol* **2020**, *8*, 21.

(6) Chen, Y.; Wang, M.; Zheng, K.; Ren, Y.; Xu, H.; Yu, Z.; Zhou, F.; Liu, C.; Qu, J.; Song, J. Antimony Nanopolyhedrons with Tunable Localized Surface Plasmon Resonances for Highly Effective Photoacoustic-Imaging-Guided Synergistic Photothermal/Immunotherapy. *Adv. Mater.* **2021**, *33*, 2100039.

(7) Runnerstrom, E. L.; Llordés, A.; Lounis, S. D.; Milliron, D. J. Nanostructured electrochromic smart windows: traditional materials and NIR-selective plasmonic nanocrystals. *Chem. Commun.* **2014**, *50*, 10555−10572.

(8) F. Carvalho, W. O.; Mejía-Salazar, J. R. Plasmonics for Telecommunications Applications. *Sensors* **2020**, *20*, 2488.

(9) Chernov, M.; Roe, A. W. Infrared neural stimulation: a new stimulation tool for central nervous system applications. *Neurophotonics* **2014**, *1*, 011011.

(10) Yoo, S.; Hong, S.; Choi, Y.; Park, J.-H.; Nam, Y. Photothermal Inhibition of Neural Activity with Near-Infrared-Sensitive Nanotransducers. *ACS Nano* **2014**, *8*, 8040−8049.

(11) Mott, M.; Koroshetz, W. Bridging the Gap in Neurotherapeutic Discovery and Development: The Role of the National Institute of Neurological Disorders and Stroke in Translational Neuroscience. *Neurotherapeutics* **2015**, *12*, 651−654.

(12) Fleischmann, M.; Hendra, P.; McQuillan, A. Raman spectra of pyridine adsorbed at a silver electrode. *Chem. Phys. Lett.* **1974**, *26*, 163−166.

(13) Lodewijks, K.; Van Roy, W.; Borghs, G.; Lagae, L.; Van Dorpe, P. Boosting the Figure-Of-Merit of LSPR-Based Refractive Index Sensing by Phase-Sensitive Measurements. *Nano Lett.* **2012**, *12*, 1655−1659.

(14) Lemos de Souza, M.; Pereira dos Santos, D.; Corio, P. Localized surface plasmon resonance enhanced photocatalysis: an experimental and theoretical mechanistic investigation. *RSC Adv.* **2018**, *8*, 28753−28762.

(15) Kelly, K. L.; Coronado, E.; Zhao, L. L.; Schatz, G. C. The Optical Properties of Metal Nanoparticles: The Influence of Size, Shape, and Dielectric Environment. *J. Phys. Chem. B* **2003**, *107*, 668−677.

(16) Khanna, P. K.; Gaikwad, S.; Adhyapak, P. V.; Singh, N.; Marimuthu, R. Synthesis and characterization of copper nanoparticles. *Mater. Lett.* **2007**, *61*, 4711−4714.

(17) Rycenga, M.; Cobley, C. M.; Zeng, J.; Li, W.; Moran, C. H.; Zhang, Q.; Qin, D.; Xia, Y. Controlling the Synthesis and Assembly of Silver Nanostructures for Plasmonic Applications. *Chem. Rev.* **2011**, *111*, 3669−3712.

(18) Amendola, V.; Pilot, R.; Frasconi, M.; Maragò, O. M.; Iatì, M. A. Surface plasmon resonance in gold nanoparticles: a review. *J. Phys.: Condens. Matter* **2017**, *29*, 203002.

(19) Gutiérrez, Y.; Brown, A. S.; Moreno, F.; Losurdo, M. Plasmonics beyond noble metals: Exploiting phase and compositional changes for manipulating plasmonic performance. *J. Appl. Phys.* **2020**, *128*, 080901.

(20) Murray, C. B.; Norris, D. J.; Bawendi, M. G. Synthesis and characterization of nearly monodisperse CdE (E = sulfur, selenium, tellurium) semiconductor nanocrystallites. *J. Am. Chem. Soc.* **1993**, *115*, 8706−8715.

(21) Luther, J. M.; Jain, P. K.; Ewers, T.; Alivisatos, A. P. Localized surface plasmon resonances arising from free carriers in doped quantum dots. *Nat. Mater.* **2011**, *10*, 361−366.

(22) Zandi, O.; Agrawal, A.; Shearer, A. B.; Reimnitz, L. C.; Dahlman, C. J.; Staller, C. M.; Milliron, D. J. Impacts of surface depletion on the plasmonic properties of doped semiconductor nanocrystals. *Nat. Mater.* **2018**, *17*, 710−717.

(23) Mock, J. J.; Barbic, M.; Smith, D. R.; Schultz, D. A.; Schultz, S. Shape effects in plasmon resonance of individual colloidal silver nanoparticles. *J. Chem. Phys.* **2002**, *116*, 6755−6759.

(24) Kovalenko, M. V.; et al. Prospects of Nanoscience with Nanocrystals. *ACS Nano* **2015**, *9*, 1012−1057.

(25) Liu, W.-D.; Yang, L.; Chen, Z.-G.; Zou, J. Promising and Eco-Friendly Cu2X-Based Thermoelectric Materials: Progress and Applications. *Adv. Mater.* **2020**, *32*, 1905703.

(26) Shi, X.-L.; Zou, J.; Chen, Z.-G. Advanced Thermoelectric Design: From Materials and Structures to Devices. *Chem. Rev.* **2020**, *120*, 7399−7515.

(27) Guo, L.; Panderi, I.; Yan, D. D.; Szulak, K.; Li, Y.; Chen, Y.-T.; Ma, H.; Niesen, D. B.; Seeram, N.; Ahmed, A.; Yan, B.; Pantazatos, D.; Lu, W. A Comparative Study of Hollow Copper Sulfide Nanoparticles and Hollow Gold Nanospheres on Degradability and Toxicity. *ACS Nano* **2013**, *7*, 8780−8793.

(28) Ghosh, S.; Avellini, T.; Petrelli, A.; Kriegel, I.; Gaspari, R.; Almeida, G.; Bertoni, G.; Cavalli, A.; Scotognella, F.; Pellegrino, T.; Manna, L. Colloidal $CuFeS_2$ Nanocrystals: Intermediate Fe d-Band Leads to High Photothermal Conversion Efficiency. *Chem. Mater.* **2016**, *28*, 4848−4858.

(29) Lee, S.; Ghosh, S.; Hoyer, C. E.; Liu, H.; Li, X.; Holmberg, V. C. Iron-Content-Dependent, Quasi-Static Dielectric Resonances and Oxidative Transitions in Bornite and Chalcopyrite Copper Iron Sulfide Nanocrystals. *Chem. Mater.* **2021**, *33*, 1821−1831.

(30) Kays, J. C.; Conti, C. R.; Margaronis, A.; Kuszynski, J. E.; Strouse, G. F.; Dennis, A. M. Controlled Synthesis and Exploration of CuxFeS4 Bornite Nanocrystals. *Chem. Mater.* **2021**, *33*, 7408−7416.

(31) Kehoe, A. B.; Scanlon, D. O.; Watson, G. W. The electronic structure of sulvanite structured semiconductors Cu_3MCh_4(M = V, Nb, Ta; Ch = S, Se, Te): prospects for optoelectronic applications. *J. Mater. Chem. C* **2015**, *3*, 12236−12244.

(32) Kehoe, A. B.; Scanlon, D. O.; Watson, G. W. Modelling potential photovoltaic absorbers Cu_3MCh_4 (M = V, Nb, Ta; Ch = S, Se, Te) using density functional theory. *J. Phys.: Condens. Matter* **2016**, *28*, 175801.

(33) Martinelli, A.; Lepore, G. O.; Bernardini, F.; Giaccherini, A.; Di Benedetto, F. The puzzling structure of Cu5FeS4 (bornite) at low temperature. *Acta Cryst. B* **2018**, *74*, 405−415.

(34) Wiltrout, A. M.; Freymeyer, N. J.; Machani, T.; Rossi, D. P.; Plass, K. E. Phase-selective synthesis of bornite nanoparticles. *J. Mater. Chem.* **2011**, *21*, 19286.

(35) Gabka, G.; Bujak, P.; Ostrowski, A.; Tomaszewski, W.; Lisowski, W.; Sobczak, J. W.; Pron, A. Cu−Fe−S Nanocrystals Exhibiting Tunable Localized Surface Plasmon Resonance in the Visible to NIR Spectral Ranges. *Inorg. Chem.* **2016**, *55*, 6660−6669.

(36) Liu, Z.; Beaulac, R. Nature of the Infrared Transition of Colloidal Indium Nitride Nanocrystals: Nonparabolicity Effects on the Plasmonic Behavior of Doped Semiconductor Nanomaterials. *Chem. Mater.* **2017**, *29*, 7507−7514.

(37) Meulenberg, R. W.; Offen, H. W.; Strouse, G. F. Low Pressure Band Tuning in Wurtzite CdSe Quantum Dots. *MRS Proceedings* **2000**, *636*, No. D9.46.1.

(38) Meulenberg, R. W.; Strouse, G. F. Pressure-induced electronic coupling in CdSe semiconductor quantum dots. *Phys. Rev. B* **2002**, *66*, 035317.

(39) Mendelsberg, R. J.; Garcia, G.; Milliron, D. J. Extracting reliable electronic properties from transmission spectra of indium tin oxide thin films and nanocrystal films by careful application of the Drude theory. *J. Appl. Phys.* **2012**, *111*, 063515.

(40) Kitagawa, Y.; Yao, H. Plasmon-Induced Polarity Inversion of Magnetic Circular Dichroism (MCD) Responses of Cu−Fe−S Bornite Nanodots upon Oxidation. *J. Phys. Chem. C* **2023**, *127*, 22149−22156.

(41) Lounis, S. D.; Runnerstrom, E. L.; Llordés, A.; Milliron, D. J. Defect Chemistry and Plasmon Physics of Colloidal Metal Oxide Nanocrystals. *J. Phys. Chem. Lett.* **2014**, *5*, 1564−1574.

(42) Runnerstrom, E. L.; Bergerud, A.; Agrawal, A.; Johns, R. W.; Dahlman, C. J.; Singh, A.; Selbach, S. M.; Milliron, D. J. Defect Engineering in Plasmonic Metal Oxide Nanocrystals. *Nano Lett.* **2016**, *16*, 3390−3398.

(43) Gibbs, S. L.; Staller, C. M.; Milliron, D. J. Surface Depletion Layers in Plasmonic Metal Oxide Nanocrystals. *Acc. Chem. Res.* **2019**, *52*, 2516−2524.

(44) Kuszynski, J. E.; Kays, J. C.; Conti, C. R.; McGill, S. A.; Dennis, A. M.; Strouse, G. F. Effective Mass for Holes in Paramagnetic, Plasmonic Cu_5FeS_4 Semiconductor Nanocrystals. *J. Phys. Chem. C* **2022**, *126*, 12669−12679.

(45) Kuszynski, J. E.; Fabiano, C. J.; Nguyen, E. T.; Mao, K.; Ahuja, A. K.; Schaller, R. D.; Strouse, G. F. Plasmon-Induced Hot-Carrier Excited-State Dynamics in Plasmonic Semiconductor Nanocrystals. *J. Phys. Chem. C* **2023**, *127*, 22654−22661.

(46) Ludwig, J.; An, L.; Pattengale, B.; Kong, Q.; Zhang, X.; Xi, P.; Huang, J. Ultrafast Hole Trapping and Relaxation Dynamics in p-Type CuS Nanodisks. *J. Phys. Chem. Lett.* **2015**, *6*, 2671−2675.

(47) Kriegel, I.; Urso, C.; Viola, D.; De Trizio, L.; Scotognella, F.; Cerullo, G.; Manna, L. Ultrafast Photodoping and Plasmon Dynamics in Fluorine−Indium Codoped Cadmium Oxide Nanocrystals for All-Optical Signal Manipulation at Optical Communication Wavelengths. *J. Phys. Chem. Lett.* **2016**, *7*, 3873−3881.

(48) Brongersma, M. L.; Halas, N. J.; Nordlander, P. Plasmon-induced hot carrier science and technology. *Nat. Nanotechnol.* **2015**, *10*, 25−34.

(49) Ghorai, N.; Ghosh, H. N. Ultrafast Plasmon Dynamics and Hole−Phonon Coupling in NIR Active Nonstoichiometric Semiconductor Plasmonic $Cu_{2-x}S$ Nanocrystals. *J. Phys. Chem. C* **2019**, *123*, 28401−28410.

(50) Lee, S. A.; Link, S. Chemical Interface Damping of Surface Plasmon Resonances. *Acc. Chem. Res.* **2021**, *54*, 1950−1960.

(51) Diroll, B. T.; Schramke, K. S.; Guo, P.; Kortshagen, U. R.; Schaller, R. D. Ultrafast Silicon Photonics with Visible to Mid-Infrared Pumping of Silicon Nanocrystals. *Nano Lett.* **2017**, *17*, 6409−6414.

(52) Giannuzzi, R.; De Donato, F.; De Trizio, L.; Monteduro, A. G.; Maruccio, G.; Scarfiello, R.; Qualtieri, A.; Manna, L. Tunable Near-Infrared Localized Surface Plasmon Resonance of F, In-Codoped CdO Nanocrystals. *ACS Appl. Mater. Interfaces* **2019**, *11*, 39921−39929.

(53) Hartstein, K. H.; Schimpf, A. M.; Salvador, M.; Gamelin, D. R. Cyclotron Splittings in the Plasmon Resonances of Electronically Doped Semiconductor Nanocrystals Probed by Magnetic Circular Dichroism Spectroscopy. *J. Phys. Chem. Lett.* **2017**, *8*, 1831−1836.

(54) Johns, R. W.; Blemker, M. A.; Azzaro, M. S.; Heo, S.; Runnerstrom, E. L.; Milliron, D. J.; Roberts, S. T. Charge carrier concentration dependence of ultrafast plasmonic relaxation in conducting metal oxide nanocrystals. *Journal of Materials Chemistry C* **2017**, *5*, 5757−5763.

(55) Hodak, J.; Martini, I.; Hartland, G. V. Ultrafast study of electron−phonon coupling in colloidal gold particles. *Chem. Phys. Lett.* **1998**, *284*, 135−141.

(56) Vincely, V. D.; Katakam, S. P.; Huda, K.; Zhong, X.; Kays, J.; Dennis, A.; Bayer, C. L. Biodegradable and biocompatible semiconductor nanocrystals as NIR-II photoacoustic imaging contrast agents. Photons Plus Ultrasound. *Proceedings of the SPIE* **2023**, *12379*, 1237915.

(57) Scotognella, F.; Della Valle, G.; Srimath Kandada, A. R.; Dorfs, D.; Zavelani-Rossi, M.; Conforti, M.; Miszta, K.; Comin, A.; Korobchevskaya, K.; Lanzani, G.; Manna, L.; Tassone, F. Plasmon Dynamics in Colloidal $Cu_{2-x}Se$ Nanocrystals. *Nano Lett.* **2011**, *11*, 4711−4717.

(58) Robie, R. A.; Seal, R. R.; Hemingway, B. S. Heat capacity and entropy of bornite (Cu_5FeS_4) between 6 and 760 K and the thermodynamic properties of phases in the system Cu-Fe-S. *Canadian Mineralogist* **1994**, *32*, 945−956.